Article

Inductive Power Transfer Battery Charger with IR-Based Closed-Loop Control

Po-Hsuan Chen * , **Chaojie Li, Zhaoyang Dong and Matthew Priestley**

School of Electrical Engineering and Telecommunications, University of New South Wales, Sydney 2052, Australia
* Correspondence: po-hsuan.chen@unsw.edu.au

Abstract: A wireless battery charger with inductive power transfer (IPT) was proposed in this paper. The commonly used constant-current constant-voltage (CC-CV) charging method is accomplished by a closed-loop controlled IPT with a hybrid resonant circuit on the secondary side. A smooth transition between the CC stage and the CV stage can be made simply by swapping exactly the associated switches on resonant capacitors. The required charging voltage and current are regulated by controlling the phase-shifted angle of the high-frequency inverter on the primary side. To stabilize the charging current and voltage, a closed-loop digital controller was introduced with infrared (IR) transmission feedback. Precise regulation of the resonant inverter on a relative small ranged phase-shifted angle can be realized by two 16-bit microcontroller units (MCUs) with compact encoding and decoding techniques. A hybrid resonant inverter was designed for a 600 W prototype of the proposed IPT battery charger. Experimental results from exemplar cases have demonstrated that the battery charger can provide a stable charging current at the CC stage and then transit smoothly into the CV stage.

Keywords: microcontrollers; inductive power transfer (IPT); phase-shift control

1. Introduction

Inductive power transfer (IPT) enables energy transfer without a metal contact interface from the source to the load [1]. The concept of convenience due to the advancement of wireless charging technologies has been expanded beyond making the electric vehicle (EV) charging process much easier. Keeping the customer safe while charging EVs is also a major factor for the growth of IPT [2]. IPT based wireless chargers can eliminate unnecessary plugins and avoid the safety issue caused by a cable-based charger device [3]. More importantly, IPT is commonly used in an environment that requires avoiding sparks such as petrol stations and cleanrooms, which is considered important for the future EV charging industry.

The power transmission efficiency of IPT wireless chargers is significantly affected by the distance between the transmitter and the receiver [4]. To improve the efficiency of energy transmission in the IPT system, resonant compensation topologies composed of inductors and capacitors are required for the loosely coupled transformer (LCT) [5]. According to the series or parallel connections of inductors and capacitors, resonant topologies can be classified into four categories: series-series (SS) [6,7], series-parallel (SP) [8], parallel-series (PS) [9], and parallel-parallel (PP) [10]. The SS resonant topology can show high efficiency in the CV mode whereas SP resonant topology can achieve a better performance in CC mode [11]. Moreover, some structures such as LLC [12] and LCC [13] are used to avoid damage to the inductors and capacitors caused by overvoltage, which can be placed on the primary side and the secondary side [14].

Several open-loop control methods for hybrid resonant circuits have been introduced for the CC-CV output requirement and aim to reduce the controller complexity [15–18]. The resonant circuit can be changed using bidirectional switches that have T and π modes

---

to adaptively match with CC or CV mode under specific conditions [15]. This hybrid structure can be configured on the primary side [16] or the secondary side. Typically, the hybrid structure is considered on the secondary side to reduce the requirement of wireless feedback by most of the literature [15]. The non-ideal property of the parasitic components and forward voltage drops leads to a significant difference between the theoretical analysis and the practical implementation of the hybrid structure. Moreover, in an open-loop control structure, the drift of the charging voltage and current during the charging process may reduce the actual charged power or damage the battery due to overcharging [19]. It is essential to develop a closed-loop control structure for IPT chargers to avoid these issues [20,21].

To achieve the closed-loop control, the design for IPT is more complex than the traditional converter as the power source of the primary side and the battery of the secondary side are physically isolated. Hence, it is necessary to develop a closed-loop control structure with wireless communication technology for transmitting and receiving the feedback signals during the charging process [22]. One of the important issues of controller design is stability consideration. There were several studies proposed to analyze and enhance the system's robustness and stability [23–26]. For example, a new small-signal analysis for a DC-DC converter with variable input and constant output has been proposed [23]. Wireless communication technologies such as power line carriers [27] and radio frequency (RF) [28] can be leveraged to transmit the feedback signal of the closed-loop control. However, it can be easily interfered by electromagnetic interference (EMI), which is caused by the electromagnetic field from the LCT or other electromagnetic signals with near frequency [29]. IR wireless communication is the optical communication technology. Optical signals would not be disturbed by electromagnetic signals. Moreover, the security of the IR communication is better because of the orientation limit between the transceiver and receiver [30].

Moreover, the transition from CC to CV mode is controlled by multiple bidirectional switches. The MOSFET-based bidirectional switch can shorten the transition time from CC to CV mode [31]. However, the total conduction loss produced by this switch can be larger than the electromechanical relay-based bidirectional switch [32]. It is also much easier to design the driver circuit for the electromechanical relay-based bidirectional switch than for the MOSFET-based one [31].

In this paper, the output drift phenomenon in practice was investigated through the experimental results and a closed-loop controller based on IR wireless communication was proposed for the hybrid IPT charger. A full-bridge inverter with phase-shift control was used to provide the AC voltage to the resonant components and transceiver coil. The required phase-shifted angle was calculated according to the battery status at the secondary side and transmitted to the primary side via IR communication. The main contributions of this paper can be summarized as follows:

(1) To address the voltage drift issue present in hybrid IPT architectures that use the simplified open-loop control strategy, a closed-loop control architecture is introduced. The voltage of the DC/AC converter is controlled by the phase-shift method [33–35]. Importantly, the required phase-shifted angle determined by the voltage and the current of the battery is computed at the secondary side and then transmitted to the primary side controller through IR wireless communication. In this case, the voltage during CV mode is not going to exceed the maximum voltage, which causes the overvoltage problem.

(2) IR is used as a wireless communication medium to carry feedback signals that can avoid the inference caused by EMI from the LCT. Furthermore, the transmitted data are not easily leaked because of the optical orientation limit, which would enhance the data security. The required phase-shifted angle was directly calculated by the microcontroller at the secondary side according to the battery voltage and current. Compared with transmitting two sets of voltage and current data, transmitting only one set of angle data can greatly reduce the time delay caused by data transmission.

The rest of the paper is organized as follows. In Section 2, the hybrid IPT charger with an IR communication-based feedback controller is introduced. The circuit characteristics under open-loop control are discussed in Section 3. In Section 4, IR is introduced as a wireless communication medium to transmit feedback signals for close-loop control. The related experiment results and the discussion is detailed in Section 5.

2. System Configuration of Hybrid IPT

The system configuration of the proposed IPT charger is shown in Figure 1. The DC resource for the LCL resonant inverter circuit comes from the AC mains through a power factor corrector. To facilitate the CC-CV charging profile, a hybrid resonant circuit was employed on the secondary side of the IPT with a full-wave rectifier. Two bidirectional switches with associated capacitors were introduced to change the topology of the resonant circuit.
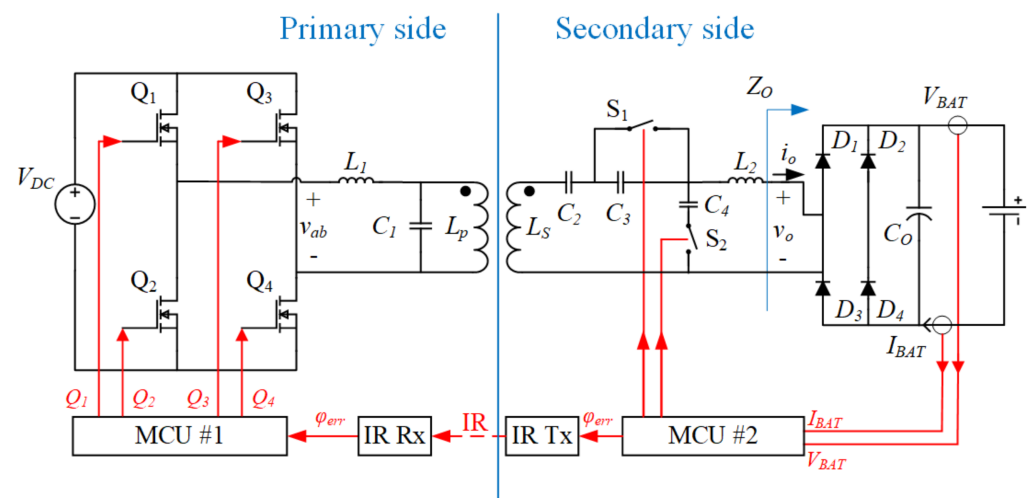

Figure 1. System configuration of the IPT charger with the hybrid resonant circuit.

Two microcontroller units (MCUs) were used in the proposed closed-loop control architecture. The MCU on the primary side (MCU #1) was used to provide phase-shift control signals for the active full-bridge inverter according to the received information transferred from the secondary side via IR communication. The MCU on the secondary side (MCU #2) was used to sample the battery charging current and voltage as well as control the two bidirectional switches. The required shifted-angle of the primary inverter would also be determined and transferred to the primary side via IR communication.

The common CC/CV charging method was used in the proposed IPT charger. The two bidirectional switches would be turned on or off for the CC or CV charging mode, as shown in Figure 1. For charging the battery in CC mode, the switches S_1 and S_2 are both turned on. Here, capacitor C_3 is bypassed, and capacitor C_4 is integrated into the compensation circuit. With this resonant compensation circuit, the charger would be able to provide a nearly constant output current, theoretically.

Once the battery voltage is increased to the rated charging voltage $V_{BAT,Max}$, the switches S_1 and S_2 will both be turned off to change the charger into the CV charging mode. The capacitor C_4 is open-circuited, and the capacitor C_3 would then be integrated into the resonant compensation circuit. Theoretically, the charger in this operation mode would be able to provide a nearly constant output voltage.

The control signals for the four active switches Q_i (i = 1, 2, 3, 4) of the inverter on the primary side and the output of the high-frequency voltage v_{ab} are shown in Figure 2, where φ is represented as the phase-shifted angle. The angular frequency of v_{ab} is defined

as ω. Specifically, the control signals for the switch pair Q_1/Q_2 (or Q_3/Q_4) in one leg are complementary. The voltage analyzed v_{ab} in Figure 2 can be given as:

$$v_{ab}(\theta) = \begin{cases} 0, & -\pi \leq \theta \leq -\pi + \left(\frac{\pi-\varphi}{2}\right) \\ -V_{DC}, & -\pi + \left(\frac{\pi-\varphi}{2}\right) \leq \theta \leq -\left(\frac{\pi-\varphi}{2}\right) \\ 0, & -\left(\frac{\pi-\varphi}{2}\right) \leq \theta \leq \left(\frac{\pi-\varphi}{2}\right) \\ V_{DC}, & \left(\frac{\pi-\varphi}{2}\right) \leq \theta \leq \pi - \left(\frac{\pi-\varphi}{2}\right) \\ 0, & \pi - \left(\frac{\pi-\varphi}{2}\right) \leq \theta \leq \pi \end{cases} \tag{1}$$

According to the Fourier transform, the output voltage v_{ab} is given as:

$$\begin{aligned} v_{ab}(\theta) &= \frac{a_0}{2} + \sum_{n=1}^{\infty} (a_n \cdot \cos(n\theta) + b_n \cdot \sin(n\theta)), -\pi \leq \theta \leq \pi \\ &= \frac{4V_{DC}}{\pi} \cos\left(\frac{\pi-\varphi}{2}\right) \sin\theta \end{aligned} \tag{2}$$

where a_0 and a_n are 0, and only the fundamental component is considered ($n = 0$). The amplitude of the inverter output voltage v_{ab} is represented as V_{ab} and can be determined by Equation (3).

$$V_{ab} = \frac{4}{\pi} V_{DC} \cdot \cos\left(\frac{\pi - \varphi}{2}\right) \tag{3}$$

where V_{DC} is represented as the input DC voltage. The amplitude of the voltage applied into the inductive power transferring circuit can be controlled by adjusting the phase-shifted angle.
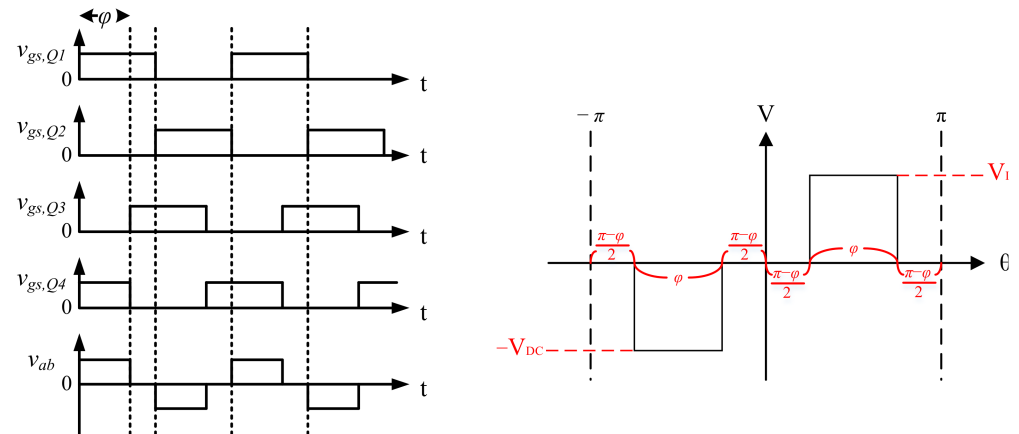

Figure 2. Waveforms of the switch control signals and primary side voltage v_{ab}.

According to the operation principles analyzed in [14], the switching frequency of the inverter should be equal to the resonant frequency of the compensation circuit to achieve the proper equivalent impedance. In Figure 2, the equivalent circuit operating in CC mode and CV mode is given, where the equivalent impedance of the diode bridge, output capacitor, and batteries is denoted as Z_o. While the charger is operated with a resonant frequency and the switches S_1 and S_2 are turned on, the charger is operated in the CC mode. The analysis of the circuit in Figure 3a is given as:

$$\begin{aligned} \vec{I_{ab}} &= j\omega C_1 \vec{V_{C_1}} + \vec{I_p} \\ &= \left\{ \left(\frac{1-\omega^2 L_p C_1}{j\omega M}\right) \left[1 - \omega C_4 \left(\frac{\omega^2 L_s C_2 - 1}{\omega C_2}\right)\right] + j\omega^3 C_1 C_4 M \right\} \cdot \vec{V_o} \\ &\quad + \left\{ j\omega L_2 \left(\frac{1-\omega^2 L_p C_1}{j\omega M}\right) + \left[j\left(\frac{\omega^2 L_2 C_2 - 1}{\omega C_2}\right)\left(\frac{1+j\omega L_p}{j\omega M}\right) - j\omega M\right] \cdot (1 - \omega^2 L_2 C_4) \right\} \vec{I_o} \end{aligned} \tag{4}$$

$$\vec{V}_{ab} = \vec{V}_{C1} + j\omega L_1 \vec{I}_p$$

$$= \left\{ \left[j\omega L_1 \left(\frac{1 - \omega^2 L_p C_1}{j\omega M} \right) + \frac{L_p}{M} \right] \left[1 - \omega C_4 \left(\frac{\omega^2 L_2 C_2 - 1}{\omega C_2} \right) \right] + \omega^2 C_4 M \left(1 - \omega^2 L_1 C_1 \right) \right\} \vec{V}_o$$

$$+ \left\{ \left\{ j \left(\frac{\omega^2 L_s C_2 - 1}{\omega C_2} \right) \left[j\omega L_1 \cdot \left(\frac{1 + j\omega L_p}{j\omega M} \right) + \frac{L_p}{M} \right] - j\omega M (j\omega L_1 + 1) \right\} \left(1 - \omega^2 L_2 C_4 \right) \right.$$

$$\left. + j\omega L_2 \left[j\omega L_1 \left(\frac{1 = \omega^2 L_p C_1}{j\omega M} \right) + \frac{L_p}{M} \right] \right\} \vec{I}_o \tag{5}$$

where the vector of the input parameter of the resonant compensated circuit is derived.
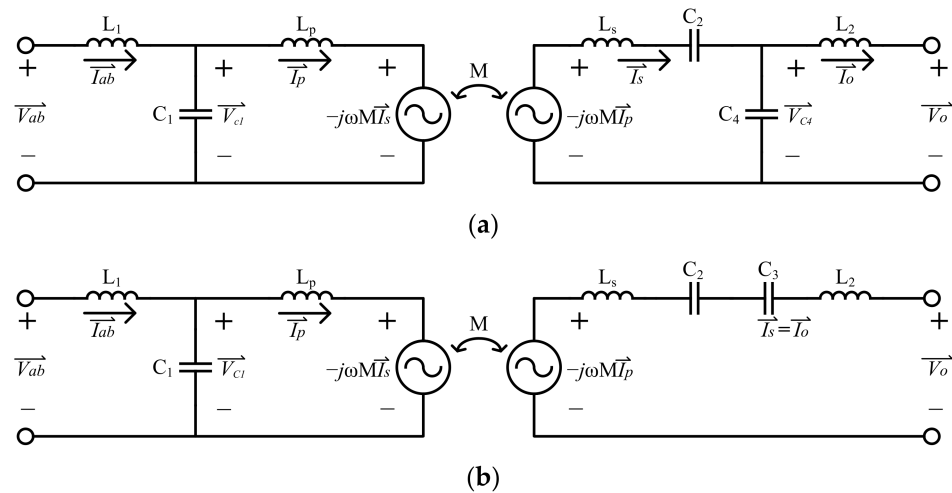

(**a**)

(**b**)

Figure 3. The equivalent circuit on the (**a**) CC output and (**b**) CV output.

The design of capacitance C_3 is equal to $C_4/2$ while the resonant frequency of the compensation circuits is expressed as Equation (6).

$$\omega = \frac{1}{\sqrt{L_1 C_1}} = \frac{1}{\sqrt{L_p C_1}} = \frac{1}{\sqrt{L_2 C_4}} = \frac{1}{\sqrt{(L_S - L_2)C_2}} \tag{6}$$

Under the condition of the resonant frequency, Equations (4) and (5) can be sorted as follows:

$$\vec{I}_{ab} = j\omega^3 C_1 C_4 M \vec{V}_o \tag{7}$$

$$\vec{V}_{ab} = j \frac{\omega L_1 L_2}{M} \cdot \vec{I}_o \tag{8}$$

According to Equation (8), it can be concluded that there is a proportional relationship between the secondary side output current and the primary side input voltage, which means that when the input voltage is fixed, the output is a stable current source, and the corresponding equivalent battery charging current can be expressed as Equation (9)

$$I_{BAT} = \frac{2I_{O,peak}}{\pi} = \frac{8}{\pi^2} \cdot \frac{MV_{ab}}{\omega L_1 L_2} = \frac{32}{\pi^3} \cdot \frac{MV_{DC} \cos\left(\frac{\pi - \varphi}{2}\right)}{\omega L_1 L_2} \tag{9}$$

where $I_{O, peak}$ is represented as the peak value of the current i_o shown in Figure 1, and M is represented as the mutual inductance of the LCT. From Equation (9), it can be seen that the battery charging current is independent of the output power.

Once switches S_1 and S_2 are turned off for the CV mode, the charger is changed to provide the CV outputs for the battery. A similar analysis of the output performance under CV mode, which is shown in Figure 3b, is listed as follows:

$$
\begin{aligned}
\vec{I}_{ab} &= j\omega C_1 \vec{V}_{C_1} + \vec{I}_p \\
&= \left(\frac{1-\omega^2 L_p C_1}{j\omega M}\right)\vec{V}_o + \left[j + \left(\frac{\omega^2 L_s C_2 - 1}{\omega C_2} + \frac{\omega^2 L_2 C_3 - 1}{\omega C_3}\right)\left(\frac{1-\omega^2 L_p C_1}{j\omega M}\right) + \omega^2 C_1 M\right]\vec{I}_s
\end{aligned}
\tag{10}
$$

$$
\begin{aligned}
\vec{V}_{ab} &= \vec{V}_{C_1} + j\omega L_1 \vec{I}_p \\
&= \left[\frac{L_1 + L_p(1-\omega^2 L_1 C_1)}{M}\right]\vec{V}_o \\
&+ \left\{\left[\frac{L_p}{M} + j\omega L_1\left(\frac{1-\omega^2 L_p C_1}{j\omega M}\right)\right]j\left(\frac{\omega^2 L_s C_2 - 1}{\omega C_2} + \frac{\omega^2 L_2 C_3 - 1}{\omega C_3}\right) - j\omega M(1-\omega^2 L_1 C_1)\right\}\vec{I}_s
\end{aligned}
\tag{11}
$$

Under the resonant circuit, the vector of the current and the voltage can be sorted as follows:

$$
\vec{I}_{ab} = \omega^2 C_1 M \vec{I}_o
\tag{12}
$$

$$
\vec{V}_{ab} = \frac{L_1}{M}\cdot\vec{V}_o
\tag{13}
$$

According to Equation (13), the relation between the output voltage and the input voltage can be derived. Hence, the charging voltage V_{BAT} is determined as Equation (14) and is independent of the output power.

$$
V_{BAT} = \frac{\pi V_{O,peak}}{4} = \frac{M V_{ab}}{L_1} = \frac{M}{L_1}\cdot V_{DC}\cdot\cos\left(\frac{\pi - \varphi}{2}\right)
\tag{14}
$$

where $V_{O,\,peak}$ is represented as the peak value of the voltage v_o shown in Figure 1. Basically, in the CC and CV modes, the charging current and voltage can be adjusted by tuning the shifted-angle of the primary side inverter.

From Equations (9) and (14), it can be seen that the charger can theoretically provide stable CC-CV output for batteries. The ideal output current and voltage expressions are both related to the phase-shifted angle. However, the parasitic elements and stray impendence of the components that appear in the practical implementation are not considered in these equations. Thus, the output voltage and current will be different from the theoretically determined values.

3. Circuit Characteristics under Open-Loop Control

To investigate the variance of the charging current and voltage from the phase-shifted angle in a practical experiment, an IPT charger with a 600 W rated output power and a hybrid compensation circuit were implemented in this study. For a common 48 V battery pack, the proposed charger can provide a maximum 10 A charging capability. Experiments of 57.8 V constant charging voltage and 10 A constant charging current were carried out, respectively. Different constant load resistances were used to simulate the battery charging load [36].

The calculated results from Equations (9) and (14) were carried out, and the experimental setup operated under open-loop control and constant resistance (CR) mode. The phase-shifted angle was tuned to reach the regulated current in CC mode or the voltage in CV mode to verify the function. To verify the prototype under open-loop condition, the resistance was chosen at 1.5 Ω, 3 Ω, and 6 Ω under CC mode, and the resistance was chosen at 6 Ω, 12 Ω, and 24 Ω under CV mode. In Figure 4a, it can be seen that to maintain a constant charging current while the charging power is increased, the phase-shifted angle should also be increased. In Figure 4b, the phase-shifted angle will be reduced to maintain

a constant output voltage, thus avoiding the battery voltage increasing continuously under CV mode. From the open-loop experimental results shown in Figure 4, it can be seen that to remain a constant charging current and voltage, there will be an angle variation of about 4° in CC mode and 10° in CV mode. Therefore, in a practical implementation of a hybrid compensated IPT charger, MCUs are required to achieve the closed-loop control by adjusting the phase-shifted angle to regulate the charging voltage and current.
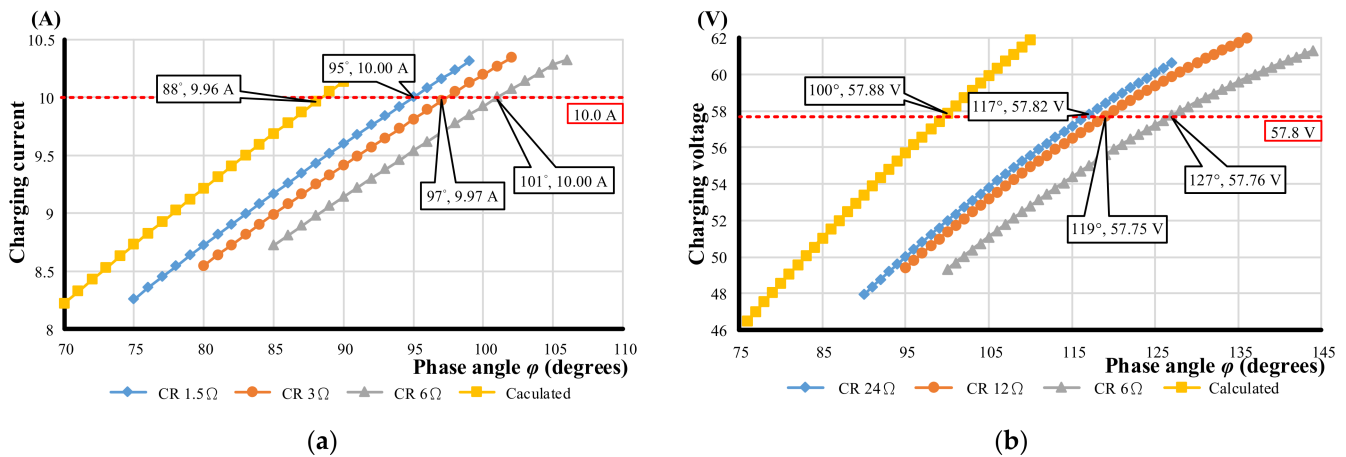
Figure 4. The phase-shifted angle and output characteristic under open-loop control with different resistance in practical and calculated results in (**a**) CC mode and (**b**) CV mode.

In this paper, an auxiliary closed-loop controller with IR wireless communication was proposed for the IPT charger to solve the issue with variations in the voltage and current from the desired values under open-loop control. MCU #2 will determine the adjustment of the phase-shifted angle according to the battery charging current and voltage. The information on adjusting the phase-shifted angle will then be transferred to the MCU #1 side via the IR communication interface. The control signals for the inverter were generated by MCU #1 based on the received information from the secondary side. As a result, the IPT charger will be able to provide a more accurate and stable charging current and charging voltage for the battery.

4. Infrared Feedback Signal Transmission Protocol and Feedback

To fulfill the charging requirement in the charging process, the closed-loop control scheme is shown in Figure 5. The sensed charging voltage and current were compared with the reference value to determine the error signals, I_{err} and V_{err}. The error signals were fed to the proportional-integral (PI) controllers to determine the corresponding phase error φ_{err}. These data were then transmitted to the primary side and a new phase-shifted angle was adjusted by MCU #1 via the received angle from the secondary side. Accordingly, the phase-shifted PWM signals of the inverter were also generated. The control signals of the bidirectional switches $S_{1,2}$ were also determined by MCU #2 according to the comparison between the reference voltage and charging voltage.
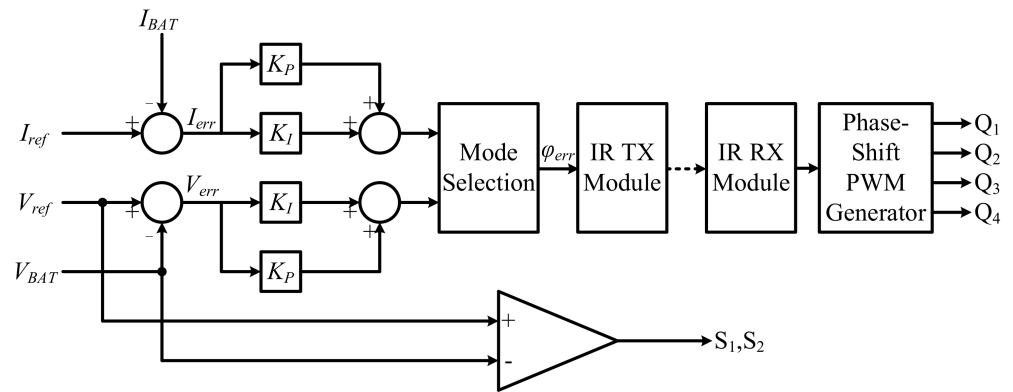
Figure 5. Closed-loop control diagram.

The control flowchart with CC-CV mode selection and phase-shifted angle is shown in Figure 6. While in CC mode, the two switches $S_{1,2}$ were turned on and the phase error φ_{err} was determined by the current error and PI controller. Once the battery pack voltage was increased to the maximum charging voltage V_{max}, the charger switched into CV mode and the two switches $S_{1,2}$ were turned off. Then, the phase error φ_{err} was determined by the voltage error and PI controller. Finally, while the charging current in the CV mode was lower than the preset minimum charging current I_{min}, the whole charging procedure was then finished.
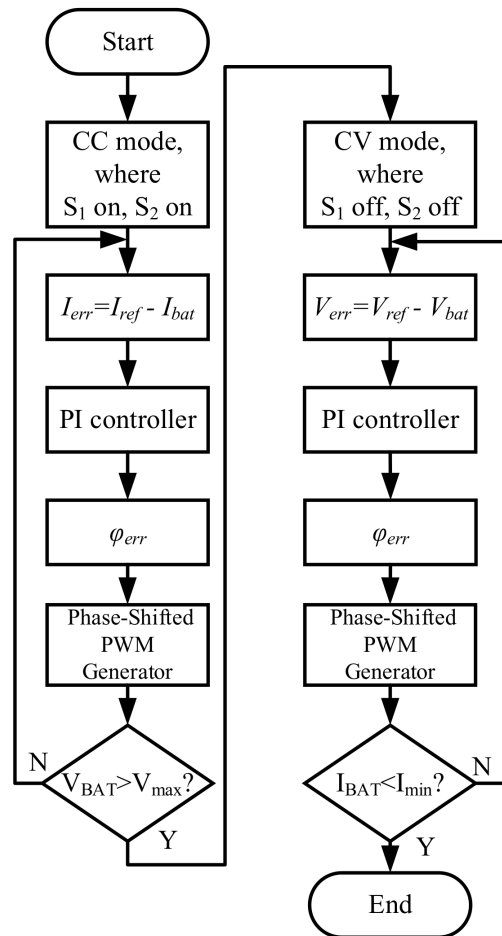

Figure 6. The control flowchart of the proposed IPT.

IR communication is a serial data transmission technology, which means that the required transmission time will increase with the number of data bits. Therefore, the dynamic response will be affected by the data transmission time. According to the protocol, the longest time of transmission a byte of data took was 14.2 ms. If the charging current and voltage are both sampled and transferred into two 10-bits data, the total transmission time to the primary side would take 28.6 ms. Hence, to reduce the required transmission time, which will facilitate a faster control response, the required phase-shifted angle was calculated from the charging voltage and current in MCU #2, as shown in Figure 5.

From the open-loop experimental results in Figure 4, to achieve the battery charging requirement, the range of phase-shifted angle φ was between about 97° and 127°. In this paper, a 16-bit microchip microcontroller dsPIC30F4011, which is common in the market, was chosen to implement the hybrid IPT charger with an IR closed-loop controller. The resolution for adjusting the φ was determined by the timer of the PWM module in the MCU. From the open-loop test in Figure 4a,b, the range of the φ was narrowed to 31°, which means that 8 bits of data are affordable to present the correct φ value. The comparison between the proposed feedback transmission method and the common strategies with two 10-bit data is shown in Table 1. Due to the transmission being changed from transmitting the charging voltage and current to φ_{err}, the amount of feedback data was reduced from 20 bits to 8 bits. The transmission time was therefore reduced to 14.2 ms, which can meet the requirement of battery charging.

Table 1. Transmission time of different protocols.

	Leader Code	**Data Code**	**Stop Code**	**Total Transmit Time**
Transmit V, I (20-bit)	3.4 ms	24.0 ms	1.2 ms	28.6 ms
Transmit φ		9.6 ms		14.2 ms

5. Experiment Results

A 600 W hardware prototype of the proposed IPT battery charger with IR closed-loop control was built. Figure 7 shows the photograph of the experimental setup including the primary side and secondary side of IPT topology, IR, and LCT coil. The size of the LCT coil including the shells was 58 mm × 58 mm × 25mm. The transmitter and receiver of the IR transmission interface were installed in the bobbins' holes on both sides. The parameters of the constructed hardware followed the design of the simulation in Table 2. The components of the semi-conductor as well as other chips are shown in Table 3. In the following experiments, the charging current command was set as 10 A in CC mode, and the charging voltage command was 57.8 V in CV mode, which is suitable for charging an electric golf cart. The corresponding phase-shifted angle in CC and CV modes can be calculated from the charging voltage and current at MCU #2.

Table 2. Parameter of passive components.

Parameter	Value
V_{DC} (Input DC voltage of power transfer)	400 V
f_O (Operating frequency)	85 kHz
d_{air} (Air gap between two coils)	2 cm
n1:n2	16:5
M (mutual inductance)	40.48 μH
L_P	175 μH
L_S	17.3 μH
L_1	180 μH
L_2	7.94 μH
C_1	19.7 nF
C_2	389.5 nF
C_3	219.0 nF
C_4	438 nF
C_O	470 μF

Table 3. Parameter of components.

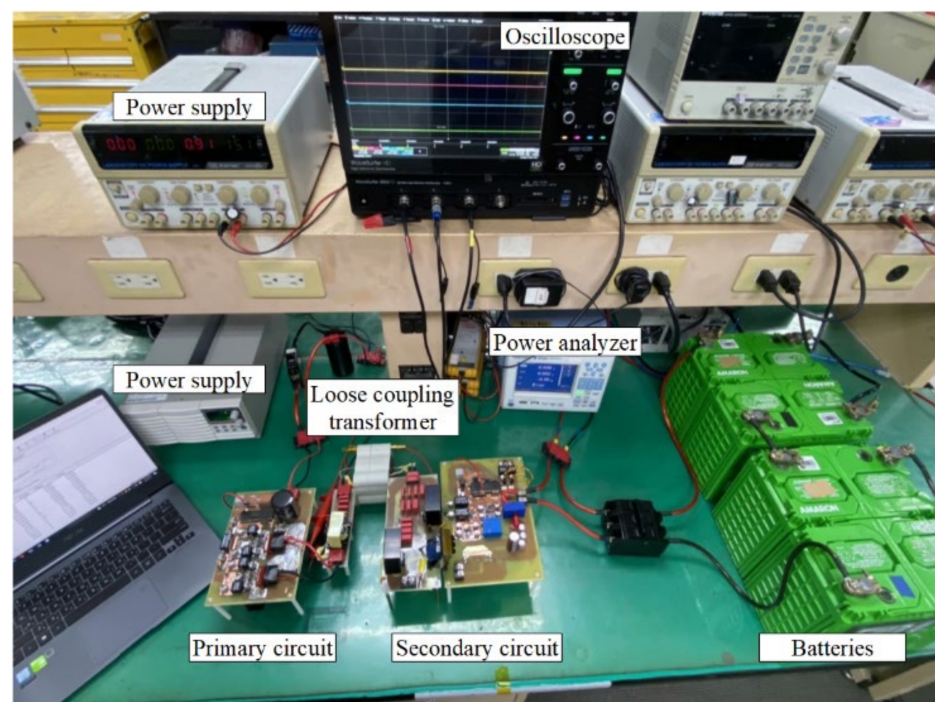| Parameter	Value/Model
MOSFETs	IXTQ36N50P
S_1, S_2	IXTQ90N20P
Diodes	DSA50C100QB
Controller	Microchip dsPIC30F4011
The model of battery	Amaron Hi life 55B24L
V_B (Battery voltage)	12 V × 4
Irate	10 A
Charging capacity	45 Ah

**Figure 7.** Experimental prototype of the proposed IPT charger.

Figure 8 shows the IR communication signals on the receiver and transmitter. The data transmission was composed of a leader code and an 8-bit data code. The delay time between Rx on the primary side and Tx on the secondary side was nearly 0.3 ms. The duration of the leader, data, and stop codes were 3.4 ms, 6.6 ms, and 1.2 ms, respectively. The total transmission time was about 11.2 ms.
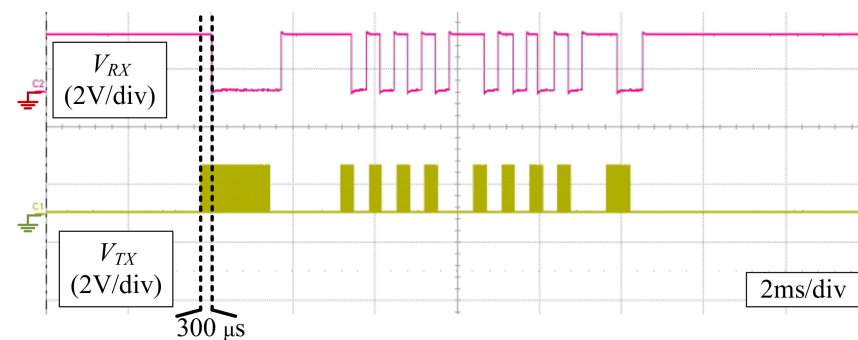
**Figure 8.** Feedback signal of infrared on the receiver and transmitter.

The waveform of the IPT configuration operated under CC mode is shown in Figure 9, and the electronic load was operated in constant power mode as a circuit load to simplify the experiment operation. In Figure 9a, the output power was about 480 W. To verify the performance of IR feedback under CC mode, Figure 9b shows the waveform when the electronic load was operated at a constant power of 600 W. The current remained at 10 A in CC mode, and the phase-shifted angle was adjusted from 101° to 104°. Figure 10 shows the transient waveforms of the IPT charger when the CC mode was switched to the CV mode. The gate drive signals $v_{gs,s1}$ and $v_{gs,s2}$ on the secondary side were switched at the same time to change charging mode from CC to CV mode. Due to the change in the configuration via switching S_1 and S_2, the phase-shifted angle should be pre-adjusted to accelerate the transition into a steady state. In Figure 10a, the current i_{L1} can be achieved to a steady state in only about 200 μs during the transition period. Figure 10b shows that both V_{BAT} and I_{BAT} can achieve a smooth transition. In Figure 11, the IPT circuit was operated under CV mode, and the charging current was gradually decreased due to the remaining CV output. During the initiation of the CV operation, the peak value of the current i_{L1} was 3.8 A while the phase-shifted angle was about 128°. As the battery was gradually charged, the phase-shifted angle was reduced to 120°, which was calculated from MCU #2 according to the charging voltage and current. The peak value of the current i_{L1} was also reduced to 1.8 A at the same time. The voltage of the battery was maintained at 57.8 V, which shows that the voltage regulation function in CV mode.

(**a**)

(**b**)
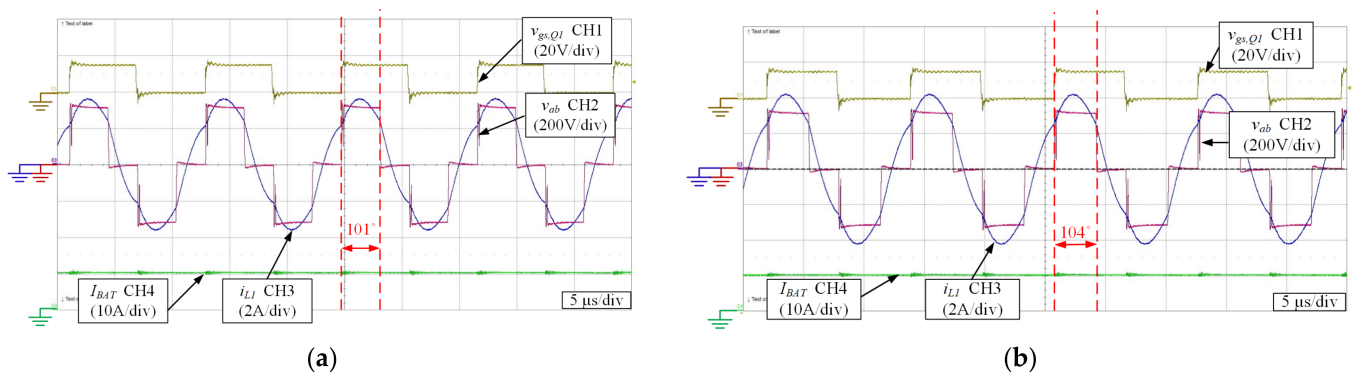
Figure 9. Experimental waveforms in CC mode and electronic load was operated in the constant power mode of (**a**) 480 W and (**b**) 600 W.


(**a**)

(**b**)
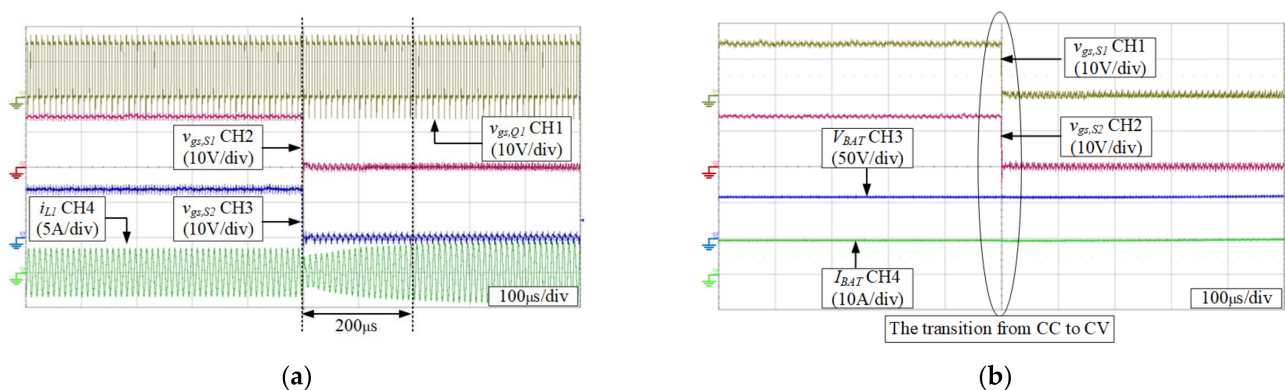
Figure 10. The transient waveforms from CC mode to CV mode: (**a**) $v_{gs,Q1}$ and i_{L1}, (**b**) V_{BAT} and I_{BAT}.
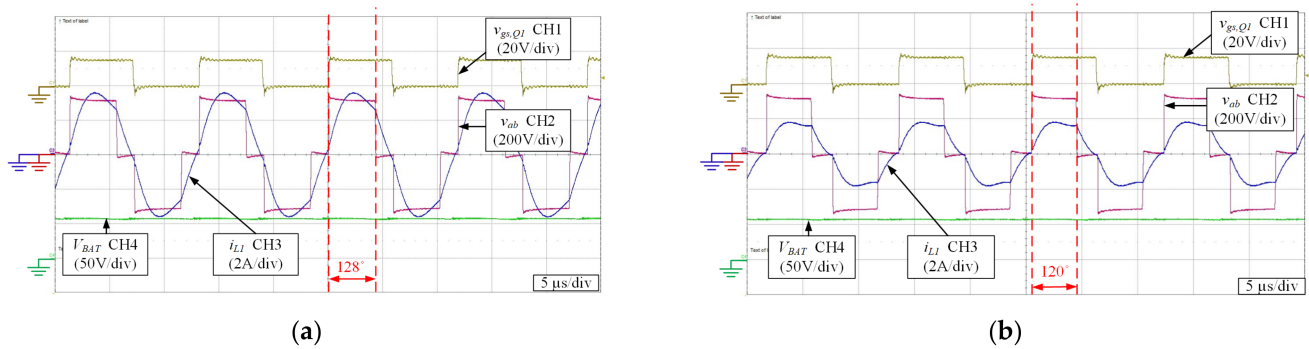
Figure 11. Experimental waveforms in CV mode and electronic load was operated in constant power mode of (**a**) 600 W and (**b**) 300 W.

In Figure 12, the efficiency was measured on the various output power with a different operation mode. It can be seen that the efficiency operating on CV mode had better performance than CC mode at the same power output. Although the number of resonant elements on the secondary side seemed to be the same in the two output modes, the conduction group of the bidirectional switch also needs to be considered in the case of constant current output. Hence, the loss in CC mode was higher than the CV mode. Furthermore, according to Equations (9) and (14), a larger phase angle to achieve the same output power is required at CC output. At the condition of the 580 W output power, the corresponding phase angle operating in CC mode was about 104° and the efficiency was 87.6%, while the corresponding phase angle operating in CV mode was about 128° and the efficiency was 90.4%.
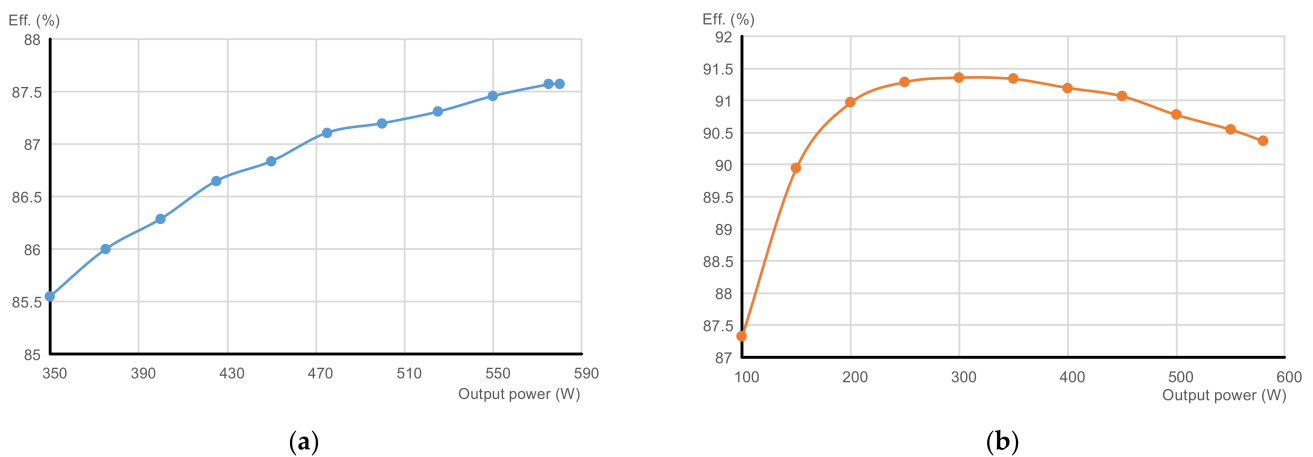
Figure 12. The efficiency operating on (**a**) CC mode and (**b**) CV mode.

To investigate the difference between the IPT charger with and without closed-loop control, both experiments on the battery charging process were carried out and recorded. An open-loop-based result is shown in Figure 13a, where the charging voltage and current drop immediately caused by the change in the circuit configuration when the mode was converted from CC to CV mode. During the CV mode, the voltage instantly dropped to 53.93 V caused by the mode transition, and then slowly rose to 55.19 V due to the continuous charging of the battery. The difference in the voltage drift between the beginning and the end of the CV mode was about 1.3 V, which cannot meet the requirement of CV charging. In Figure 13b, the charging voltage of the closed-loop-based design can remain at a constant value of 57.8 V during the transient time from CC mode to CV mode. Compared with the open-loop-based design, the charging current can be maintained at a constant in CC mode and the charging voltage can be kept constantly in CV mode. On the other hand, the

smooth conversion from CC mode to CV mode is unable to be achieved under open-loop control.
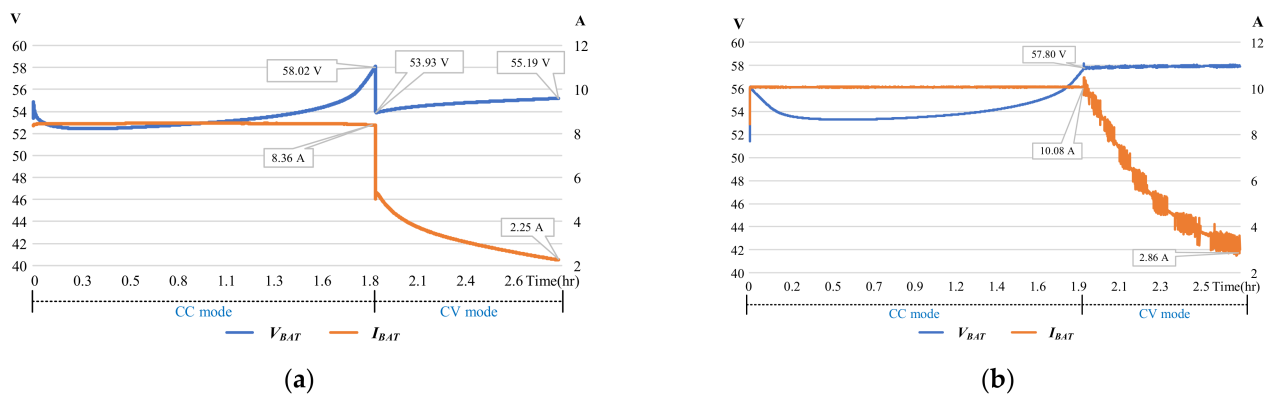
Figure 13. Measured charging process of the battery under (**a**) open-loop and (**b**) closed-loop.

6. Conclusions

An IPT charger with hybrid resonant compensation and IR closed-loop controller was introduced in this paper. The hybrid resonant compensation was used to provide constant current and constant voltage output characteristics. However, according to the experimental analysis of the battery charger, it can be seen that it does not seem possible to remain the CC-CV output with only open-loop control. A wireless closed-loop controller with IR communication was proposed to solve this issue. The IR communication technology was used for data transmission between the primary and secondary sides. Optical communication signals would not be easily disturbed by electromagnetic signals. Moreover, the security was better because of the orientation limit between the transceiver and receiver. In practice, the open-loop control method led to variations in the battery current and voltage from the desired values due to the losses caused by the non-ideal characteristic of electric components. These variations resulted in a non-optimal charging profile for the battery and transient excursions past the rated current and voltage values. A 600 W IPT charger for a 48 V 45 Ah battery was implemented to verify the validity and performance of the proposed charger. From the experimental results, it can be seen that the charging current and voltage errors can be greatly improved. It shows that the IPT charger with IR developed in this paper can be applied to charging electrical golf carts.

References

1. Ruddell, S.I.; Madawala, U.K.; Thrimawithana, D.J. A Wireless EV Charging Topology With Integrated Energy Storage. *IEEE Trans. Power Electron.* **2020**, *35*, 8965–8972. [CrossRef]
2. Takura, T.; Matsuki, H. Relationship Between Drive Frequency and Load Characteristics in Bidirectional Contactless Power Transfer for Electric Vehicles. *IEEE Trans. Magn.* **2018**, *54*, 1–5. [CrossRef]

3. Zhang, Z.; Pang, H.; Georgiadis, A.; Cecati, C. Wireless Power Transfer–An Overview. *IEEE Trans. Ind. Electron.* **2019**, *66*, 1044–1058. [CrossRef]
4. Dai, J.; Ludois, D.C. A Survey of Wireless Power Transfer and a Critical Comparison of Inductive and Capacitive Coupling for Small Gap Applications. *IEEE Trans. Power Electron.* **2015**, *30*, 6017–6029. [CrossRef]
5. Qu, X.; Chu, H.; Wong, S.-C.; Tse, C.K. An IPT Battery Charger With Near Unity Power Factor and Load-Independent Constant Output Combating Design Constraints of Input Voltage and Transformer Parameters. *IEEE Trans. Power Electron.* **2018**, *34*, 7719–7727. [CrossRef]
6. Vardani, B.; Tummuru, N.R. A Single-Stage Bidirectional Inductive Power Transfer System With Closed-Loop Current Control Strategy. *IEEE Trans. Transp. Electrification* **2020**, *6*, 948–957. [CrossRef]
7. Mostafa, A.; Wang, Y.; Zhang, H.; Zhu, C.; Mei, Y.; Jiao, N.; Lu, F. Output Power Regulation of a Series-Series Inductive Power Transfer System Based on Hybrid Voltage and Frequency Tuning Method for Electric Vehicle Charging. *IEEE Trans. Ind. Electron.* **2022**, *69*, 9927–9937. [CrossRef]
8. Sohn, Y.H.; Choi, B.H.; Lee, E.S.; Lim, G.C.; Cho, G.-H.; Rim, C.T. General Unified Analyses of Two-Capacitor Inductive Power Transfer Systems: Equivalence of Current-Source SS and SP Compensations. *IEEE Trans. Power Electron.* **2015**, *30*, 6030–6045. [CrossRef]
9. Samanta, S.; Rathore, A.K. Wireless power transfer technology using full-bridge current-fed topology for medium power applications. *IET Power Electron.* **2016**, *9*, 1903–1913. [CrossRef]
10. Hatchavanich, N.; Sangswang, A.; Konghirun, M. Secondary-Side Voltage Control via Primary-Side Controller for Wireless EV Chargers. *IEEE Access* **2020**, *8*, 203543–203554. [CrossRef]
11. Song, K.; Li, Z.; Jiang, J.; Zhu, C. Constant Current/Voltage Charging Operation for Series-Series and Series-Parallel Compensated Wireless Power Transfer Systems Employing Primary-Side Controller. *IEEE Trans. Power Electron.* **2017**, *33*, 8065–8080. [CrossRef]
12. Hsieh, H.-I.; Wang, H.; Huang, T.-H. LLC Charger Using Quasi-Contactless Power Transfer by Resonant Magnetic Induction Coupling. *IEEE Trans. Transp. Electrification* **2018**, *4*, 376–388. [CrossRef]
13. Feng, H.; Cai, T.; Duan, S.; Zhao, J.; Zhang, X.; Chen, C. An LCC-Compensated Resonant Converter Optimized for Robust Reaction to Large Coupling Variation in Dynamic Wireless Power Transfer. *IEEE Trans. Ind. Electron.* **2016**, *63*, 6591–6601. [CrossRef]
14. Mai, J.; Sun, X.; Wang, Y.; Gu, P.; Zeng, X.; Wu, K.; Yao, Y.; Xu, D. Analysis, Design, and Optimization of the IPT System With LC Filter Rectifier Featuring High Efficiency. *IEEE Trans. Ind. Electron.* **2021**, *69*, 12829–12841. [CrossRef]
15. Wang, D.; Qu, X.; Yao, Y.; Yang, P. Hybrid Inductive-Power-Transfer Battery Chargers for Electric Vehicle Onboard Charging With Configurable Charging Profile. *IEEE Trans. Intell. Transp. Syst.* **2020**, *22*, 592–599. [CrossRef]
16. Qu, X.; Han, H.; Wong, S.-C.; Tse, C.K.; Chen, W. Hybrid IPT Topologies With Constant Current or Constant Voltage Output for Battery Charging Applications. *IEEE Trans. Power Electron.* **2015**, *30*, 6329–6337. [CrossRef]
17. Li, G.; Ma, H. Hybrid IPT system with natural CC–CV output characteristics for EVs battery charging applications. *IET Power Electron.* **2020**, *13*, 3734–3743. [CrossRef]
18. Qu, X.; Yao, Y.; Wang, D.; Wong, S.-C.; Tse, C.K. A Family of Hybrid IPT Topologies With Near Load-Independent Output and High Tolerance to Pad Misalignment. *IEEE Trans. Power Electron.* **2019**, *35*, 6867–6877. [CrossRef]
19. Pai, K.-J. Depressing Start-Up Current Overshoot for a Laser Headlight Driver in High-Temperature and Forward Voltage Drift Conditions. *IEEE Trans. Ind. Electron.* **2018**, *65*, 7793–7804. [CrossRef]
20. Feng, H.; Lukic, S.M. Reduced-Order Modeling and Design of Single-Stage LCL Compensated IPT System for Low Voltage Vehicle Charging Applications. *IEEE Trans. Veh. Technol.* **2020**, *69*, 3728–3739. [CrossRef]
21. Samanta, S.; Rathore, A.K. Small-Signal Modeling and Closed-Loop Control of a Parallel–Series/Series Resonant Converter for Wireless Inductive Power Transfer. *IEEE Trans. Ind. Electron.* **2018**, *66*, 172–182. [CrossRef]
22. Huang, Z.; Lam, C.-S.; Mak, P.-I.; Martins, R.P.D.S.; Wong, S.-C.; Tse, C.K. A Single-Stage Inductive-Power-Transfer Converter for Constant-Power and Maximum-Efficiency Battery Charging. *IEEE Trans. Power Electron.* **2020**, *35*, 8973–8984. [CrossRef]
23. Wu, Y.; Huangfu, Y.; Ma, R.Y.; Ravey, A.; Chrenko, D. A Strong Robust DC-DC Converter of All-Digital High-Order Sliding Mode Control for Fuel Cell Power Applications. *J. Power Sources.* **2019**, *413*, 222–232. [CrossRef]
24. Wu, Y.; Wang, Z.; Huangfu, Y.; Ravey, A.; Chrenko, D.; Gao, F. Hierarchical Operation of Electric Vehicle Charging Station in Smart Grid Integration Applications—An Overview. *Int. J. Electr. Power Energy Syst.* **2022**, *139*, 108005. [CrossRef]
25. Wu, Y.; Ravey, A.; Chrenko, D.; Miraoui, A. Demand Side Energy Management of EV Charging Stations by Approximate Dynamic Programming. *Energy Convers. Manag.* **2019**, *196*, 878–890. [CrossRef]
26. Wu, Y.; Zhang, J.; Ravey, A.; Chrenko, D.; Miraoui, A. Real-Time Energy Management of Photovoltaic-Assisted Electric Vehicle Charging Station by Markov Decision Process. *J. Power Sources.* **2020**, *476*, 228504. [CrossRef]
27. Sanftl, B.; Joffe, C.; Trautmann, M.; Weigel, R.; Koelpin, A. Reliabe data link for power transfer control in an inductive charging system for electric vehicles. In Proceedings of the 2016 IEEE MTT-S International Conference on Microwaves for Intelligent Mobility (ICMIM), San Diego, CA, USA, 19–20 May 2016; pp. 1–3. [CrossRef]
28. Zheng, C.; Lai, J.-S.; Chen, R.; Faraci, W.E.; Zahid, Z.U.; Gu, B.; Zhang, L.; Lisi, G.; Anderson, D. High-Efficiency Contactless Power Transfer System for Electric Vehicle Battery Charging Application. *IEEE J. Emerg. Sel. Top. Power Electron.* **2014**, *3*, 65–74. [CrossRef]

29. Hong, S.; Kim, Y.; Lee, S.; Jeong, S.; Sim, B.; Kim, H.; Song, J.; Ahn, S.; Kim, J. A Frequency-Selective EMI Reduction Method for Tightly Coupled Wireless Power Transfer Systems Using Resonant Frequency Control of a Shielding Coil in Smartphone Application. *IEEE Trans. Electromagn. Compat.* **2019**, *61*, 2031–2039. [CrossRef]

30. Gati, E.; Kampitsis, G.; Manias, S. Variable Frequency Controller for Inductive Power Transfer in Dynamic Conditions. *IEEE Trans. Power Electron.* **2016**, *32*, 1684–1696. [CrossRef]

31. Chub, A.; Vinnikov, D.; Kosenko, R.; Liivik, E.; Galkin, I. Bidirectional DC–DC Converter for Modular Residential Battery Energy Storage Systems. *IEEE Trans. Ind. Electron.* **2019**, *67*, 1944–1955. [CrossRef]

32. Yepes, A.G.; Doval-Gandoy, J.; Toliyat, H.A. Strategy With Smooth Transitions and Improved Torque–Speed Region and Stator Copper Loss for Two-Level Asymmetrical Six-Phase Induction Motor Drives Under Switch Faults. *IEEE Trans. Power Electron.* **2020**, *36*, 1954–1969. [CrossRef]

33. Deng, Q.; Wang, Z.; Chen, C.; Czarkowski, D.; Kazimierczuk, M.K.; Zhou, H.; Hu, W. Modeling and Control of Inductive Power Transfer System Supplied by Multiphase Phase-Controlled Inverter. *IEEE Trans. Power Electron.* **2018**, *34*, 9303–9315. [CrossRef]

34. Zhang, Y.; Chen, S.; Li, X.; Tang, Y. Dual-Side Phase-Shift Control of Wireless Power Transfer Implemented on Primary Side Based on Driving Windings. *IEEE Trans. Ind. Electron.* **2021**, *68*, 8999–9002. [CrossRef]

35. Zhang, Y.; Li, X.; Chen, S.; Tang, Y. Soft Switching for Strongly Coupled Wireless Power Transfer System With 90° Dual-Side Phase Shift. *IEEE Trans. Ind. Electron.* **2022**, *69*, 282–292. [CrossRef]

36. Huang, Z.; Wong, S.-C.; Tse, C.K. Design of a Single-Stage Inductive-Power-Transfer Converter for Efficient EV Battery Charging. *IEEE Trans. Veh. Technol.* **2016**, *66*, 5808–5821. [CrossRef]